The Cryosphere Discuss., 7, 4913–4936, 2013
www.the-cryosphere-discuss.net/7/4913/2013/
doi:10.5194/tcd-7-4913-2013
© Author(s) 2013. CC Attribution 3.0 License.

The Cryosphere Discussions
Open Access

This discussion paper is/has been under review for the journal The Cryosphere (TC).
Please refer to the corresponding final paper in TC if available.

Transition of flow regime along a marine-terminating outlet glacier in East Antarctica

D. Callens[1], K. Matsuoka[2], D. Steinhage[3], B. Smith[4], and F. Pattyn[1]

[1]Laboratoire de Glaciologie, Université Libre de Bruxelles, Brussels, Belgium
[2]Norwegian Polar Institute, Tromsø, Norway
[3]Alfred-Wegener-Institut Helmholtz-Zentrum für Polar- und Meeresforschung, Bremerhaven, Germany
[4]Applied Physics Laboratory, University of Washington, Seattle, WA, USA

Received: 10 September 2013 – Accepted: 23 September 2013 – Published: 7 October 2013

Correspondence to: D. Callens (dcallens@ulb.ac.be)

Published by Copernicus Publications on behalf of the European Geosciences Union.

Abstract

We present results of a multi-methodological approach to characterize the flow regime of West Ragnhild Glacier, the widest glacier in Dronning Maud Land, Antarctica. A new airborne radar survey points to substantially thicker ice (> 2000 m) than previously thought. According to the new data, West Ragnhild Glacier discharges 13–14 Gt yr^{-1}. Therefore, it is one of the three major outlet glaciers in Dronning Maud Land. Glacier-bed topography is distinct between the upstream and downstream section. In the downstream section (< 65 km upstream of the grounding line), the glacier overlies a wide and flat basin well below the sea level while the upstream region is more mountainous. Spectrum analysis of the bed topography reveals a clear contrast between these two regions, suggesting that the downstream area is sediment covered. The bed returned power varies by 30 dB within 20 km near the bed flatness transition, which suggests that water content at bed/ice interface increases over a short distance downstream, hence pointing to water-rich sediment. Ice flow speed observed in the downstream part of the glacier (∼ 250 m yr^{-1}) can only be explained if basal motion accounts for ∼ 60 % of the surface motion. All above lines of evidence (sediment bed, wetness and basal motion) and the relative flat grounding zone give the potential for West Ragnhild Glacier to be more sensitive to external forcing compared to other major outlet glaciers in this region which are more stable due to their bed geometry (e.g. Shirase Glacier).

1 Introduction

The overall mass balance of the Antarctic ice sheet is dominated by a significant mass deficit in West Antarctica (Rignot et al., 2008; Pritchard et al., 2012), while the East-Antarctic ice sheet is only slightly losing mass, as increased surface accumulation compensates mass loss through outlet glaciers (Shepherd et al., 2012). The distinct West-Antarctic mass deficit is primarily due to thinning and acceleration of glaciers, leading to an increased mass flux across the grounding line. Glacier acceleration has

TCD
7, 4913–4936, 2013

been observed for most West-Antarctic glaciers draining the Amundsen Sea Sector (e.g., Pine Island Glacier; Joughin et al., 2003) and in the Antarctic Peninsula (Scambos et al., 2004). Such accelerations are usually associated with loss of buttressing from ice shelves (Schoof, 2010). However the way glaciers react to ice loss largely depends on their geometry as well as their subglacial conditions (Schoof, 2007b; Hulbe et al., 2008).

Such loss of buttressing from ice shelves and subsequent mass loss is not observed in the East-Antarctic ice sheet. It is currently believed that the East-Antarctic ice sheet is much more stable than its West-Antarctic counterpart. The main reason for this difference is that West Antarctica is a marine ice sheet and its contact with the ocean makes it potentially more vulnerable. However, limited observations in Dronning Maud Land (DML), East Antarctica, show that the ice sheet seaward of the inland mountains lies on a bed well below the sea level (BEDMAP2; Fretwell et al., 2013) and most of the ice from the polar plateau is discharged through numerous glaciers in between coastal mountain ranges. The ice-dynamical consequence of such settings are not yet explored. In this paper we investigate the marine boundary of the East-Antarctic ice sheet in DML and its potential for a more dynamic response than is currently observed.

The coastal region of DML, East Antarctica, is characterized by numerous outlet glaciers feeding into ice shelves that extend more than 1000 km along the coast (Fig. 1a). These ice shelves are generally short in length but reach up to the continental shelf. The stability of these ice shelves is primarily ensured through the presence of ice rises and pinning points, making the ice shelf locally grounded. Potential unpinning of these ice shelves would inevitably lead to ice shelf speed up, which makes them sensitive to marine forcing.

Of all glaciers in DML, the West Ragnhild Glacier is the widest (≈ 90 km) and longest one (ice speed is already 100 m yr^{-1} 250 km away of the grounding line), flowing into the Roi Baudouin Ice Shelf. Based on the ice thickness data presented in this paper, we estimate the grounding line mass flux to be 13–14 Gt yr^{-1}, which constitutes roughly 10 % of the total discharge from DML (Rignot et al., 2008). This is of the same order of

TCD
7, 4913–4936, 2013

magnitude as Shirase Glacier ($13.8 \pm 1.6\,\mathrm{Gt\,yr^{-1}}$; Pattyn and Derauw, 2002) and Jutulstraumen ($14.2\,\mathrm{Gt\,yr^{-1}}$; Høydal, 1996), the other two major outlet glaciers in the DML region. The stability of the West Ragnhild Glacier is most likely governed by the dynamics of its ice shelf which is characterized by two important ice rises and several pinning points. While rapid changes at the marine boundary have not yet been observed, Rignot et al. (2013) point to an exceedance of basal melt (underneath the ice shelf and at the grounding line) over calving for several ice shelves in DML (including Roi Baudouin Ice Shelf, downstream of the West Ragnhild Glacier). Melting at the grounding line 50 km west from West Ragnhild Glacier has been reported in Pattyn et al. (2012), but its magnitude is of the orders of tens of centimetres per year.

To understand what makes the West Ragnhild Glacier one of the three most significant mass outputs in DML, we investigated its basal conditions using satellite interferometry, airborne radar and ice-sheet modelling. First, radar analysis reveals the geometry of the bed. Second, we characterize the roughness of the bed and its reflectivity through spectrum and bed returned power analyses, which inform us on the nature of the bed as well as on the water content. Finally, we compare surface velocity obtained by satellites with modelled velocities using an ice sheet flow model, leading to a characterization of areas where basal motion/sliding should subsist. We subsequently discuss the consequences of a marine-terminating East-Antarctic outlet glacier, characterized by a wet sediment and dominated by basal motion/sliding.

2 Data acquisition

Ice flow surface velocities were generated based on RADARSAT data acquired during the austral spring of 2000. These velocities combine phase and speckle-tracking offsets, using methods that minimize the error of the final combined product (Joughin, 2002). The resolution of the velocity data is 500 m × 500 m, covering the main trunk of the West Ragnhild Glacier and its vicinity (Fig. 1b).

TCD
7, 4913–4936, 2013

The airborne radio-echo sounding survey was carried out on West Ragnhild Glacier during the austral summer 2010–2011, resulting in one longitudinal (along-flow) profile and seven cross profiles (Fig. 1b). The radar system employs a 150 MHz center frequency and transmits bursts of 600 ns and 60 ns duration, toggling between the two bursts (Nixdorf et al., 1999; Steinhage et al., 2001). The system records at a rate of 20 Hz. For further signal to noise improvement, the data of same burst length are ten fold stacked, resulting in a horizontal resolution of 80 ± 20 m. We identified the bed echo along 91 % of the entire survey (Fig. 2). Most sections lacking a bed echo are shorter than ∼ 10 km (the maximum data gap is 20 km). Adjacent regions to these data gaps are sloping down steeply toward the data gaps. Therefore, these data gaps probably correspond to a low bed and thick ice, causing an increased radar signal attenuation, and which may explain the loss of signal.

Ice thickness was derived using a constant radio-wave propagation speed of 168 m μs^{-1}. Surface elevation is obtained by laser altimetry from the aircraft, and bed elevation is subsequently derived by subtracting the ice thickness from the surface elevation. We applied the geoid height of 20 m above the EGM96 ellipsoid (Rapp, 1997) to derive the surface and bed elevations relative to the sea level.

3 Mapping the subglacial topography

The radar survey reveals bedrock topography that is significantly different from previous estimates (Lythe et al., 2001)[1]. Furthermore, the survey highlights a marked contrast in bed topography (Fig. 2). Between the Sør Rondane and Belgica Mountains, ice flows in a deeply incised valley, ∼ 20 km wide lying ∼ 1000 m below sea level at the two uppermost cross profiles (Fig. 2b). The bed topography is rather variable here, fluctuating between 1200 and 800 m b.s.l. Further downstream, bedrock elevation in-

[1]The data collected for this paper are incorporated in the recently published BEDMAP2 dataset (Fretwell et al., 2013).

TCD
7, 4913–4936, 2013

creases rapidly (more than 500 m within 10 km distance) up to a flat subglacial lowland lying around 600 m b.s.l. This can be observed on both the longitudinal (Fig. 2a) and cross profiles (Fig. 2b). The elevation of this lowland varies less than 50 m locally, so the lowland is much flatter than the landward valley between Sør Rondane and Belgica Mountains. The amplitude of the local elevation variations increases sharply between cross profiles 4 and 5 as we reach the piedmont of the Sør Rondane Mountains. This is also the zone where we found the onset of the subglacial valley, described earlier.

4 Spectral analysis of bed topography

4.1 Bed roughness index

One way to quantitatively characterize the above-described bed conditions is to calculate bed roughness. The bed roughness index *RI* is obtained by applying a Fast Fourier Transform (FFT) to the bed elevation within a moving window (Taylor et al., 2004):

$$RI = \int_{f_{\min}}^{f_{\max}} \frac{|X[f]|^2}{N_T \Delta x} \mathrm{d}f, \quad (1)$$

where $f_{\min} = 1/(N_T \Delta x)$, $f_{\max} = 1/(2\Delta x)$, $N_T = 2^n$ is the number of data points in the window, Δx is the sampling interval (100 m in our case) and where

$$X[f] = \sum_{d=1}^{N_T} x(d) e^{\frac{2\pi i}{N_T}(d-1)(f-1)}. \quad (2)$$

Equation (2) is the definition of the FFT for a dataset $x(d)$ with index d in the range $1 \le d \le N_T$, and $X[f]$ is the same dataset in the frequency domain with index f in the range $f_{\min} \le f \le f_{\max}$. In other words, the bed roughness index *RI* is the integral of the resultant power spectrum within each of the moving windows.

TCD
7, 4913–4936, 2013

We first resampled the radar-derived bed topography (80 ± 20 m intervals) with a fixed (100 m) interval. We then detrended the measured bed elevation in each moving window, which is required to perform a FFT. The method was applied within a 2^n data point window. Several authors recommend $n \geq 5$ (Taylor et al., 2004; Bingham and Siegert, 2009; Rippin et al., 2011). By using $n = 6$ we were able to analyse roughness over wavelengths ranging from 200 up to 6400 m.

4.2 Results

The longitudinal bed profile (Fig. 2) reveals two distinct areas: a flat area (between the grounding line and 65 km upstream) and an intersected subglacial relief typical of subglacial mountain ranges. The transition between them occurs within 10 km. The bed roughness index *RI* is capable of quantifying this difference (Figs. 3 and 4a). While the two regions are still quite distinct, the transition of roughness from one to the other is smoother. For the downstream cross profiles, the bed is rougher away from the current glacier flowline (longitudinal radar profile). The low roughness area is therefore restricted to the zones of fast ice flow. Once outside this section, bed roughness indices increase, pointing to a less smooth surface. Following the analysis of Bingham and Siegert (2009), the flat and smooth area in the downstream section of the West Ragnhild Glacier may therefore very well be overlain by sediment, in contrast to bedrock further upstream, characterized by higher roughness indexes.

5 Analysis of bed-returned power

5.1 Analytical setup

To further examine the spatial distribution of the basal conditions, we analysed the radar power returned from the bed, hereafter called *BRP*. The geometrically corrected *BRP*, BRP^c, can be seen as a proximal bed reflectivity if englacial effects are removed adequately (Matsuoka, 2011). The BRP^c is affected by both englacial attenuation *L* and

TCD
7, 4913–4936, 2013

bed reflectivity R. In decibel scale, $[x]_{\mathrm{dB}} = 10\log_{10}(x)$, this relationship can be written as:

$$[BRP^{c}]_{\mathrm{dB}} = [BRP]_{\mathrm{dB}} + 10\log_{10}\left(h + \frac{H}{n}\right)^{2},$$
$$\simeq [R]_{\mathrm{dB}} - [L]_{\mathrm{dB}}\,. \quad (3)$$

The geometrically corrected bed returned power BRP^{c} can be calculated based on the measured BRP returned from the bed and a geometric factor defined by $(h+H/n)^2$. Here, h is the height of the aircraft above the glacier surface, H is the ice thickness (distance between the surface and the bed of the ice mass), and n is the refraction index of the ice (~ 1.8; Matsuoka et al., 2012). The BRP^{c} is then normalized to the mean of the observed values.

One has to note that effects of temporal changes in the instrumental characteristics and of ice-crystal alignments are ignored in Eq. (3). Englacial attenuation has contributions from pure ice and chemical constituents included in the glacier ice, both of which depend exponentially on ice temperature. Although the chemical contribution to attenuation can nearly equal the pure-ice contribution near the coast (Matsuoka et al., 2012), the lack of observation forces us to ignore its contribution and to use only the pure-ice contribution to estimate englacial attenuation.

To model englacial attenuation we estimate the temperature fields associated with the steady-state flow field calculated using a higher-order flowline model (see Sect. 6 for a model description). We estimate attenuation L from the modelled temperature fields using Eqs. (4)–(6) listed below (Matsuoka et al., 2012). The depth-average attenuation rate $\langle N \rangle$ is derived from the depth profile of the attenuation rate $N(z)$, i.e.,

$$[L]_{\mathrm{dB}} = \int_{0}^{H} N(z)\,\mathrm{d}z\,. \quad (4)$$

TCD
7, 4913–4936, 2013

The attenuation profile $N(z)$ is proportional to local ice conductivity σ:

$$N(z) = \frac{1000(10\log_{10}e)}{c\,\varepsilon_0\sqrt{\varepsilon}}\sigma(z) \approx 0.914\,\sigma(z)\,, \tag{5}$$

where c is the wave velocity in vacuum, ε_0 is the permittivity of free space and ε is the relative permittivity of the ice. Since we focus only on the contribution of pure ice to the attenuation, conductivity depends only on temperature through an Arrhenius-type relationship.

$$\sigma = \sigma_0 \exp\left[-\frac{E_0}{k}\left(\frac{1}{T(z)} - \frac{1}{T_r}\right)\right], \tag{6}$$

where $\sigma_0 = 15.4\,\mu\mathrm{S\,m^{-1}}$ is the pure-ice conductivity at the reference temperature $T_r = 251\,\mathrm{K}$, $T(z)$ is the vertical profile of temperature, $E_0 = 3.8\,\mathrm{keV}$ is the activation energy and $k = 8.617 \times 10^{-5}\,\mathrm{eV\,K^{-1}}$ is the Boltzmann constant (Matsuoka et al., 2012). The temperature fields is derived from the ice-flow model experiments A, B and C (see Sect. 6). Figure 4c shows $[L]$ along the longitudinal profile. Despite the differences in boundary conditions that govern the three temperature fields, results are similar for all of them, which emphasizes the robustness of the method.

5.2 Results

In the upstream valley, BRP^c remains relatively low (−20 dB) and varies little (several dB) except at two sites where BRP^c shows anomalous features (90 km and 170 km upstream from the grounding line; Fig. 4b). Further downstream, BRP^c increases by ∼ 50 dB within 20 km, over which the ice thins only by ∼ 200 m (Fig. 2).

To clarify contributions of the bed reflectivity on BRP^c, we estimated the englacial attenuation using predicted temperature (Fig. 4c). Attenuation decreases ∼ 20 dB within 10 km at 65 km upstream from the grounding line. Further downstream, attenuation gradually decreases by 20 dB over 50 km, which is probably more related to the

TCD
7, 4913–4936, 2013

changes in ice thickness than to changes in depth-averaged attenuation rate $\langle N \rangle$. To retrieve the actual bed reflectivity, we estimated bed reflectivity from BRP^c and englacial attenuation using Eq. (3). The corresponding estimated bed reflectivity rapidly increases, approaching the grounding line at 40–50 km, from where it varies little within the last ~ 30 km (Fig. 4d). The high bed reflectivity in the zone immediately upstream of the grounding line may eventually point to wet bed conditions. This high bed reflectivity is not directly related to the smoother bed interface because *RI* is calculated for the wavelengths longer than 200 m but the reflectivity is affected by the bed smoothness in the scale of several wavelengths of the radio wave (5 m for this study). In the next section, we will investigate whether wet basal conditions are likely or not.

6 Ice-flow modeling

6.1 Model setup

Interferometric analysis of satellite synthetic-aperture radar data shows that West Ragnhild Glacier accelerates steadily towards the grounding line (Fig. 5). Here, we want to determine what fraction of this flow speed will solely be contributed by ice deformation, hence what fraction should be due to basal sliding/motion. Therefore, we modelled ice deformation diagnostically (i.e., steady state force balance and velocity field for a fixed present day geometry) along the center flowline (shown in Fig. 1a) using a higher-order flowline model, which takes into account both longitudinal stress gradients and vertical shearing (Pattyn, 2002; Pattyn et al., 2005, 2006). A similar approach was taken by Rippin et al. (2003) in their analysis of Bailey and Slessor basins, based on a simplified model compared to the higher-order model approach.

The surface and bed topography within the survey domain are taken from our data. Beyond this domain, bed and surface topography are taken from both BEDMAP (Lythe et al., 2001) and Bamber et al. (2009). The resulting profile is similar to the one resam-

TCD
7, 4913–4936, 2013

pled directly from BEDMAP2 (Fretwell et al., 2013), since our ice thickness data has been included.

Short gaps within the retrieved bed echoes are linearly interpolated; the length of such gaps is typically less than several ice thicknesses, so that the large-scale flow fields are hardly affected by this choice. Longer gaps were interpolated in the same way. Bed topography uncertainties associated with the longer data gaps induces flow-speed uncertainties in the most upstream area and are sufficiently far away of our region of interest.

Besides surface and basal topography, basic inputs for the ice flow model are surface mass balance, which is derived from van de Berg et al. (2006), and geothermal heat flux. Since the purpose of the experiments is to determine the spatial variability of basal motion according to the difference between deformational and observed surface velocity, basal velocity is set to zero as a lower boundary condition to the flow field. Further boundary conditions are a zero horizontal ice velocity at the ice divide and a fixed depth-averaged velocity at the grounding line, derived from satellite measurements, i.e., $250\,\mathrm{m\,yr^{-1}}$.

Full thermomechanical coupling of the ice flow to temperature, which requires solving for the free surface, was not performed. Instead we relied on procedure described in Pattyn (2010) and Pattyn et al. (2012), this allows us to perform diagnostic run of the model and use the observed surface topography. Therefore, we assumed that the flow parameter is uniform and calculated the flow fields for five different temperature-dependent flow parameter values. Each of the values corresponds to mean ice temperatures of −2, −4, −5, −10, and −15 °C (Cuffey and Paterson, 2010).

For each ice-flow field derived for a uniform flow parameter, we derived corresponding ice temperature field and use it to estimate englacial attenuation. We use a geothermal heat flux of $42\,\mathrm{mW\,m^{-2}}$ as lower boundary condition. However, the actual basal temperature gradient may probably be higher because of the presence of sediment, reaching values of $60\,\mathrm{mW\,m^{-2}}$ or more (e.g. Shapiro and Ritzwoller, 2004; Fox-Maule et al., 2005). However, the exact choice of geothermal heat flux will not affect the mod-

TCD
7, 4913–4936, 2013

elled englacial attenuation since the bed in the surveyed domain is predicted to be at the pressure melting point everywhere even with a flux as low as 42 mW m^{-2}. Once the bed reaches pressure melting point, additional geothermal and shear heating has virtually no impact on ice temperature, hence on englacial attenuation (Matsuoka, 2011). Therefore, the estimated along-flow patterns of the attenuation and bed reflectivity are robust regardless of the uncertainties in geothermal heat flux.

6.2 Results

Amongst the five different flow parameters depicted in Fig. 5, case A corresponds to the warmest (softest) ice (−2 °C), and predicts higher ice flow speeds due to ice deformation in the upstream region. Cases B and C display deformation patterns similar to A, but better match the observed surface velocities in the upstream region (> 100 km). Cases D and E correspond to much colder (stiffer) ice (−10 and −15 °C, respectively) and predict deformational velocities that are too small compared to the observed ones. The best fitting cases B and C, and to a lesser extent case A, are also within the most plausible temperature range for Antarctic englacial ice (Cuffey and Paterson, 2010).

Cases A, B, and C consistently show the same pattern of deformational velocity along the flowline. Over the thickest section of the longitudinal profile, ice motion is essentially governed by internal deformation, and a good match can be obtained for a series of different englacial temperatures. We interpret that the mismatch between satellite measured surface flow speed and the modelled ice deformation velocity is mainly due to the basal motion of the glacier, irrespective of the softness/hardness of the ice. All experiments show that basal motion is dominant only in the downstream region, though exact onset of the basal flow depends on the cases (50–100 km upstream of the grounding line).

Nevertheless, the imposed fixed velocity boundary condition at the grounding line strongly affects model results within ∼ 10 km of the grounding line, as can be seen in Fig. 5, because the flow speed of the ice at the base changes from zero to a non-zero value within one grid point. No-slip/slip boundary conditions are quite common in

TCD
7, 4913–4936, 2013

numerical ice sheet experiments (Hindmarsh, 1993) and all the model experiment show a similar sharp increase in flow speed from some distance upstream of the grounding line to the grounding line. This discrepancy is notably due to the lack of basal motion in the model, which furthermore underscores the present-day observed velocity in the downstream section, basal sliding is an essential factor, accounting for up to 60 % of the total velocity.

7 Discussion

Prior to our study, only two glaciers were considered as important contributors to discharge ice from DML, i.e., Jutulstraumen and Shirase Glacier, and both have been the subject of more interest in the past (e.g. Høydal, 1996; Pattyn and Derauw, 2002). Despite their fast flow (the grounding-line velocity of Shirase Glacier is $> 2000\,\mathrm{m\,yr^{-1}}$), they each discharge approximately 10 % of the total snow accumulation of this part of the ice sheet (Rignot et al., 2008). Both glaciers are topographically constrained and characterized by a highly convergent flow regime. They also terminate in a relatively narrow trunk. From an ice-dynamical viewpoint, Shirase Glacier is a relatively stable feature, as its grounding line cannot retreat over a distance larger than 5 to 10 km, since the bedrock rapidly rises above sea level from the present position of the grounding line (Pattyn, 1996, 2000; Pattyn and Derauw, 2002). Such conditions make an outlet glacier less prone to dynamic grounding line retreat and significant mass loss due to dynamic changes in the ice shelf.

The new data on West Ragnhild Glacier definitely changes the discharge picture in DML; the substantially thicker ice leads to a higher flux into the ice shelf, compared to previous estimates (Rignot and Thomas, 2002; Rignot et al., 2011a). Based on the new thickness data across the grounding line in conjunction with interferometric ice flow velocities, its discharge ($13–14\,\mathrm{Gt\,yr^{-1}}$) is comparable to the discharge of Jutulstraumen and Shirase Glacier. Nonetheless, ice flow velocities of West Ragnhild Glacier are relatively low. Ice flow speed is $> 100\,\mathrm{m\,yr^{-1}}$ at 100 km upstream of the grounding line,

TCD
7, 4913–4936, 2013

and up to 250 m yr^{-1} at the grounding line (Fig. 1). The reason for such low values is ice-shelf buttressing by two major ice rises within the Roi Baudouin Ice Shelf, slowing down the flow upstream. While according to Rignot et al. (2008), the area seemed to be in balance, a significant imbalance is currently observed in the grounding zone of West Ragnhild Glacier and along the grounding line of the Roi Baudouin ice shelf (Rignot et al., 2013), which is in line with direct observations (Pattyn et al., 2012).

Despite present-day stable conditions, the analysis presented in this paper clearly demonstrates that West Ragnhild Glacier (i) is an important outlet glacier, (ii) is marine terminating with a grounding line 600–700 m b.s.l., and (iii) has a downstream section that is smooth, sediment covered and water saturated for at least 65 km upstream of the grounding line. Given the fact that the smooth bed is also flat and horizontal and devoid of distinct lateral constraints, the grounding line is potentially capable of advancing and retreating across a substantial area. According to theoretical considerations (Schoof, 2007a), a grounding-line retreat may be expected if sudden changes would occur at the seaward side. This setting is comparable to the Siple Coast ice streams, where soft-bedded ice streams are buttressed by the Ross Ice Shelf and ice rises such as Roosevelt Island. The close proximity of the DML ice shelves to the margin of the continental shelf (Timmermann et al., 2010, and Fig. 1a) could potentially allow relatively warm water from the abyssal plains to circulate under the shelf, leading to significant sub-shelf melting (e.g., Smedsrud et al., 2006). Unpinning of the ice shelf could therefore lead to grounding line retreat due to increased flow speed, hence increased dynamic mass loss, in line with recent observations (Rignot et al., 2013). New geophysical data presented in this paper highlight such possibility in West Ragnhild Glacier, which discharges 10 % of ice from the DML sector.

8 Conclusions

Based on an extensive airborne radar campaign, new bed data show compelling evidence that the West Ragnhild glacier is one of the main discharge features of the ice

TCD
7, 4913–4936, 2013

sheet in DML. Despite its low ice velocities at the grounding line, its ice flux across the grounding line is equally significant compared to the other main outlet glaciers Jutulstraumen and Shirase Glacier, each of them discharging approximately 10 % of the ice sheet in this sector.

The lowermost 65 km of the the West Ragnhild Glacier lies on a smooth bed, which is presumably covered with sediment and its lateral position is little constrained by the topography. In view of its flatness across the glacier, the bed has little lateral topographic constraints, albeit that it is laterally restricted to the fast-flowing sector of the ice stream. Analysis of the radar power returned from the bed and bed topography spectrum shows that this area is likely sediment-covered and water saturated. Englacial temperature modelling reveals that the bed along the entire glacier is at pressure melting point, irrespective of a wide range of boundary conditions applied. Ice-flow modelling has demonstrated that within this section, basal motion accounts for about 60 % of the surface motion of the glacier.

Acknowledgements. The radar survey was conducted by the Alfred Wegener Institute with further logistical support from the Princess Elisabeth Station (Belgian Antarctic Research Expedition, BELARE), and funded by the European Facilities for Airborne Research (EUFAR). DC is funded through a FNRS–FRIA fellowship (Fonds de la Recherche Scientifique) and an Yggdrasil mobility grant (Research Council of Norway). This work is in part supported by the Center for Ice, Climate and Ecosystems (ICE) at the Norwegian Polar Institute.

References

Bamber, J. L., Gomez-Dans, J. L., and Griggs, J. A.: A new 1 km digital elevation model of the Antarctic derived from combined satellite radar and laser data – Part 1: Data and methods, The Cryosphere, 3, 101–111, doi:10.5194/tc-3-101-2009, 2009. 4922, 4932

Bindschadler, R. A., Choi, H., and ASAID Collaborators: High-Resolution Image-derived Grounding and Hydrostatic Lines for the Antarctic Ice Sheet, Digital media, National Snow and Ice Data Center, Boulder, Colorado, USA, 2011. 4932

TCD
7, 4913–4936, 2013

Bingham, R. G. and Siegert, M. J.: Quantifying subglacial bed roughness in Antarctica: implications for ice-sheet dynamics and history, Quaternary Sci. Rev., 28, 223–236, 2009. 4919
Cuffey, K. and Paterson, W. S. B.: The Physics of Glaciers, 4th edn., Elsevier, New York, 2010. 4923, 4924, 4936
Fox-Maule, C., Purucker, M. E., Olsen, N., and Mosegaard, K.: Heat flux anomalies in Antarctica revealed by satellite magnetic data, Science, 309, 464–467, 2005. 4923
Fretwell, P., Pritchard, H. D., Vaughan, D. G., Bamber, J. L., Barrand, N. E., Bell, R., Bianchi, C., Bingham, R. G., Blankenship, D. D., Casassa, G., Catania, G., Callens, D., Conway, H., Cook, A. J., Corr, H. F. J., Damaske, D., Damm, V., Ferraccioli, F., Forsberg, R., Fujita, S., Gim, Y., Gogineni, P., Griggs, J. A., Hindmarsh, R. C. A., Holmlund, P., Holt, J. W., Jacobel, R. W., Jenkins, A., Jokat, W., Jordan, T., King, E. C., Kohler, J., Krabill, W., Riger-Kusk, M., Langley, K. A., Leitchenkov, G., Leuschen, C., Luyendyk, B. P., Matsuoka, K., Mouginot, J., Nitsche, F. O., Nogi, Y., Nost, O. A., Popov, S. V., Rignot, E., Rippin, D. M., Rivera, A., Roberts, J., Ross, N., Siegert, M. J., Smith, A. M., Steinhage, D., Studinger, M., Sun, B., Tinto, B. K., Welch, B. C., Wilson, D., Young, D. A., Xiangbin, C., and Zirizzotti, A.: Bedmap2: improved ice bed, surface and thickness datasets for Antarctica, The Cryosphere, 7, 375–393, doi:10.5194/tc-7-375-2013, 2013. 4915, 4917, 4923
Hindmarsh, R. C. A.: Qualitative dynamics of marine ice sheets, in: Ice in the Climate System, edited by: Peltier, W., NATO ASI Series I (12), Springer-Verlag, Berlin, 67–99, 1993. 4925
Høydal, Ø. A.: A force-balance study of ice flow and basal conditions of Jutulstraumen, Antarctica, J. Glaciol., 42, 413–425, 1996. 4916, 4925
Hulbe, C. L., Scambos, T. A., Youngberg, T., and Lamb, A. K.: Patterns of glacier response to disintegration of the Larsen B ice shelf, Antarctica Peninsula, Global Planet. Change, 63, 1–8, 2008. 4915
Joughin, I.: Ice-sheet velocity mapping: a combined interferometric and speckle-tracking approach, Ann. Glaciol., 34, 195–201, 2002. 4916
Joughin, I., Rignot, E., Rosanova, C. E., Lucchitta, B. K., and Bohlander, J.: Timing of Recent Accelerations of Pine Island Glacier, Antarctica, Geophys. Res. Lett., 30, 1706, doi:10.1029/2003GL017609, 2013. 4915
Lythe, M. B., Vaughan, D. G., and BEDMAP consortium: BEDMAP: a new ice thickness and subglacial topographic model of Antarctica, J. Geophys. Res., 106, 11335–11351, 2001. 4917, 4922

TCD
7, 4913–4936, 2013

Matsuoka, K.: Pitfalls in radar diagnosis of ice-sheet bed conditions: Lessons from englacial attenuation models, Geophys. Res. Lett., 38, L05505, doi:10.1029/2010GL046205, 2011. 4919, 4924
Matsuoka, K., MacGregor, J. A., and Pattyn, F.: Predicting radar attenuation within the Antarctic ice sheet, Earth Planet. Sc. Lett., 359–360, 173–183, 2012. 4920, 4921
Nixdorf, U., Steinhage, D., Meyer, U., Hempel, L., Jenett, M., Wachs, P., and Miller, H.: The newly developed airborne radio-echo sounding system of the AWI as a glaciological tool, Ann. Glaciol., 29, 231–238, 1999. 4917
Pattyn, F.: Numerical modelling of a fast-flowing outlet glacier: experiments with different basal conditions, Ann. Glaciol., 23, 237–246, 1996. 4925
Pattyn, F.: Ice-sheet modelling at different spatial resolutions: focus on the grounding line, Ann. Glaciol., 31, 211–216, 2000. 4925
Pattyn, F.: Transient glacier response with a higher-order numerical ice-flow model, J. Glaciol., 48, 467–477, 2002. 4922
Pattyn, F.: Antarctic subglacial conditions inferred from a hybrid ice sheet/ice stream model, Earth Planet. Sc. Lett., 295, 451–461, 2010. 4923
Pattyn, F. and Derauw, D.: Ice-dynamic conditions of Shirase Glacier, Antarctica, inferred from ERS–SAR interferometry, J. Glaciol., 48, 559–565, 2002. 4916, 4925
Pattyn, F., De Brabander, S., and Huyghe, A.: Basal and thermal control mechanisms of the Ragnhild glaciers, East Antarctica, Ann. Glaciol., 40, 225–231, 2005. 4922
Pattyn, F., Huyghe, A., De Brabander, S., and De Smedt, B.: Role of transition zones in marine ice sheet dynamics, J. Geophys. Res., 111, F02004, doi:10.1029/2005JF000394, 2006. 4922
Pattyn, F., Matsuoka, K., Callens, D., Conway, H., Depoorter, M., Docquier, D., Hubbard, B., Samyn, D., and Tison, J. L.: Melting and refreezing beneath Roi Baudouin Ice Shelf (East Antarctica) inferred from radar, GPS, and ice core data, J. Geophys. Res., 117, F04008, doi:10.1029/2011JF002154, 2012. 4916, 4923, 4926
Pritchard, H. D., Ligtenberg, S. R. M., Fricker, H. A., Vaughan, D. G., van den Broeke, M. R., and Padman, L.: Antarctic ice-sheet loss driven by basal melting of ice shelves, Nature, 484, 502–505, doi:10.1038/nature10968, 2012. 4914
Rapp, R. H.: Use of potential coefficient models for geoid undulation determinations using a spherical harmonic representation of the height anomaly/geoid undulation difference, J. Geodesy, 71, 282–289, 1997. 4917

TCD
7, 4913–4936, 2013

Rignot, E. J. and Thomas, R. H.: Mass balance of polar ice sheets, Science, 297, 1502–1506, 2002. 4925
Rignot, E. J., Bamber, J. L., van den Broeke, M. R., Davis, C., Li, Y., van de Berg, W. J., and van Meijgaard, E.: Recent Antarctic ice mass loss from radar interferometry and regional climate modelling, Nat. Geosci., 1, 106–110, 2008. 4914, 4915, 4925, 4926
Rignot, E., Mouginot, J., and Scheuchl, B.: Ice flow of the Antarctic ice sheet, Science, 333, 1427–1430, 2011a. 4925, 4932
Rignot, E., Mouginot, J., and Scheuchl, B.: MEaSUREs Antarctic Grounding Line from Differential Satellite Radar Interferometry, NASA EOSDIS Distributed Active Archive Center at NSIDC, Boulder, Colorado, USA, Digital media, 2011b. 4932
Rignot, E., Jacobs, S., Mouginot, J., and Scheuchl, B.: Ice shelf melting around Antarctica, Science, 314, 266–270, 2013. 4916, 4926
Rippin, D. M., Bamber, J. L., Siegert, M. J., Vaughan, D. G., and Corr, H. F. J.: Basal topography and ice flow in the Bailey/Slessor region of East Antarctica, J. Geophys. Res., 108, 6008, doi:10.1029/2003JF000039, 2003. 4922
Rippin, D. M., Vaughan, D. G., and Corr, H. F. J.: The basal roughness of Pine Island Glacier, West Antarctica, J. Glaciol., 57, 67–76, 2011. 4919
Scambos, T. A., Bohlander, J. A., Shuman, C. A., and Skvarca, P.: Glacier acceleration and thinning after ice shelf collapse in the Larsen B embayment, Antarctica, Geophys. Res. Lett., 31, L18402, doi:10.1029/2004GL020670, 2004. 4915
SCAR: Scientific Committee on Antarctic Research Antarctic Digital Datablase, available at: http://www.add.scar.org, digital media, last access: 06/07/2012, 2012. 4932
Schoof, C.: Ice sheet grounding line dynamics: steady states, stability and hysteresis, J. Geophys. Res., 112, F03S28, doi:10.1029/2006JF000664, 2007a. 4926
Schoof, C.: Marine ice sheet dynamics. Part 1: The case of rapid sliding, J. Fluid Mech., 573, 27–55, 2007b. 4915
Schoof, C.: Glaciology: beneath a floating ice shelf, Nat. Geosci., 3, 450–451, 2010. 4915
Shapiro, N. M. and Ritzwoller, M. H.: Inferring surface heat flux distributions guided by a global seismic model: particular application to Antarctica, Earth Planet. Sc. Lett., 223, 213–224, 2004. 4923
Shepherd, A., Ivins, E. R., Geruo, A., Barletta, V. R., Bentley, M. J., Bettadpur, S., Briggs, K. H., Bromwich, D. H., Forsberg, R., Galin, N., Horwath, M., Jacobs, S., Joughin, I., King, M. A., Lenaerts, J. T. M., Li, J., Ligtenberg, S. R. M., Luckman, A., Luthcke, S. B., McMillan, M.,

TCD
7, 4913–4936, 2013

Meister, R., Milne, G., Mouginot, J., Muir, A., Nicolas, J. P., Paden, J., Payne, A. J., Pritchard, H., Rignot, E., Rott, H., Sandberg Sørensen, L., Scambos, T. A., Scheuchl, B., Schrama, E. J. O., Smith, B., Sundal, A. V., van Angelen, J. H., van de Berg, W. J., van den Broeke, M. R., Vaughan, D. G., Velicogna, I., Wahr, J., Whitehouse, P. L., Wingham, D. J., Yi, D., Young, D., and Zwally, H. J.: A reconciled estimate of ice-sheet mass balance, Science, 338, 1183–1189, 2012. 4914

Smedsrud, L. H., Jenkins, A., Holland, D. M., and Nøst, O. A.: Modeling ocean processes below Fimbulisen, Antarctica, J. Geophys. Res., 111, C01007, doi:10.1029/2005JC002915, 2006. 4926

Steinhage, D., Nixdorf, U., Meyer, U., and Miller, H.: Subglacial topography and internal structure of central and western Dronning Maud Land, Antarctica, determined from airborne radio echo sounding, J. Appl. Geophys., 47, 183–189, 2001. 4917

Taylor, J., Siegert, M., Payne, A., and Hubbard, B.: Regional-scale bed roughness beneath ice masses: measurement and analysis, Comput. Geosci., 30, 899–908, 2004. 4918, 4919

Timmermann, R., Le Brocq, A., Deen, T., Domack, E., Dutrieux, P., Galton-Fenzi, B., Hellmer, H., Humbert, A., Jansen, D., Jenkins, A., Lambrecht, A., Makinson, K., Niederjasper, F., Nitsche, F., Nøst, O. A., Smedsrud, L. H., and Smith, W. H. F.: A consistent data set of Antarctic ice sheet topography, cavity geometry, and global bathymetry, Earth Syst. Sci. Data, 2, 261–273, doi:10.5194/essd-2-261-2010, 2010. 4926

van de Berg, W. J., van den Broeke, M. R., Reijmer, C. H., and van Meijgaard, E.: Reassessment of the Antarctic surface mass balance using calibrated output of a regional atmospheric climate model, J. Geophys. Res., 111, D11104, doi:10.1029/2005JD006495, 2006. 4923

TCD
7, 4913–4936, 2013

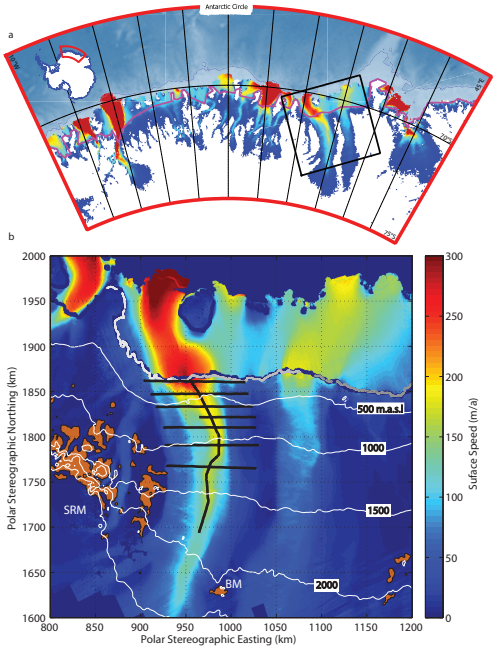

Fig. 1. Overview map of West Ragnhild Glacier, Dronning Maud Land, East Antarctica. **(a)** Dronning Maud Land. Ice-flow speed is shown on the same scale as for panel **(b)** (but white when $< 15\,m\,yr^{-1}$ Rignot et al., 2011a). The grounding line is shown in purple (Bindschadler et al., 2011). Rock outcrops are shown in brown (SCAR, 2012). The square shows the 400 km × 400 km area covered by the map on panel **(b)**. The inset shows the coverage of the panel **(a)**. **(b)** West Ragnhild Glacier. Background color shows the surface flow speed derived from satellite interferometry and speckle-tracking. Contours show surface elevations at 500 m interval (Bamber et al., 2009). From West to East, the grounding line is defined from a couple of PALSAR imagery taken in 2007 (light grey) and from 2 pairs of RADARSAT (middle grey and dark grey) in 2000 (Rignot et al., 2011b). Black lines are the longitudinal and cross radar profiles. Rock outcrops as in **(a)**.

TCD
7, 4913–4936, 2013

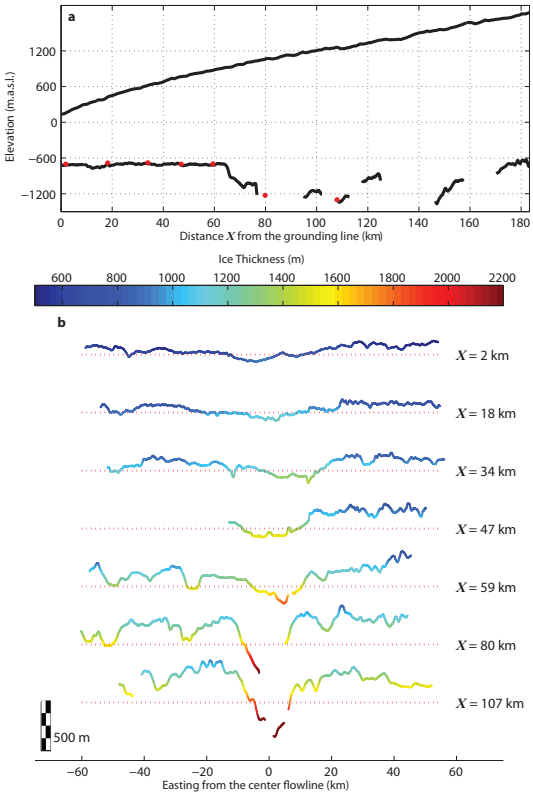

Fig. 2. Radar data. **(a)** Ice and bed topography along the central flowline. The seven red circles are the locations of the cross profiles. **(b)** Bed topography (ordinate) and ice thickness (color) measured across the flow. The red dotted lines show the isodepth of 600 m b.s.l., the approximate elevation of the flat basin measured along the center flowline **(a)** and the reference for each profile. Distance along each cross profile (right) is measured from the grounding line.

TCD
7, 4913–4936, 2013

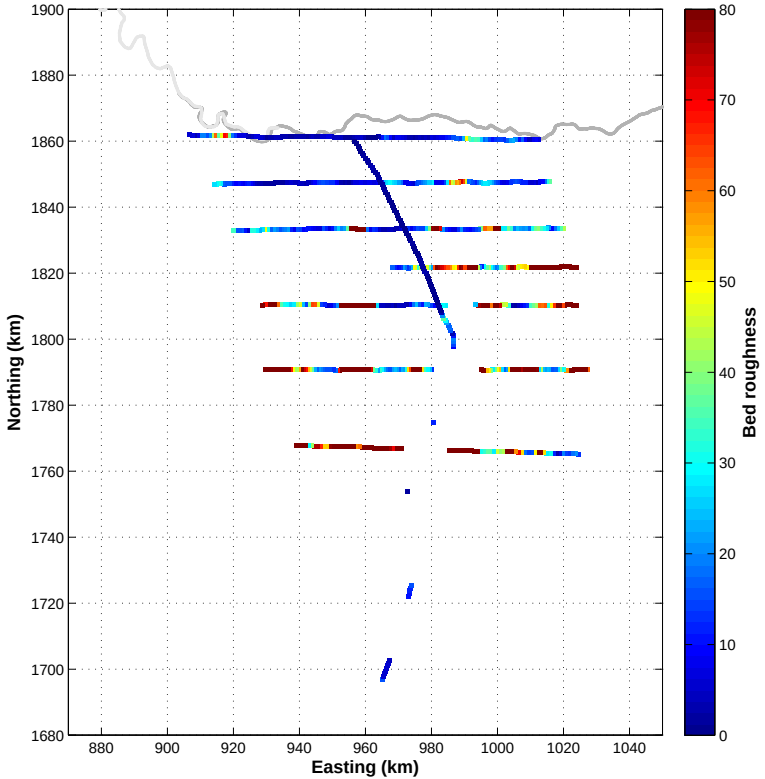

Fig. 3. Bed roughness analysis. Bed roughness index of the basal topography (color) calculated for wavelengths ranging from 200 to 6400 m. The grounding line is the same as in Fig. 1b. Short legs of absent bed echoes results in long gaps of the estimated bed roughness indices due the window-based calculation of the bed roughness index. Larger *RI* refers rougher bed.

TCD
7, 4913–4936, 2013

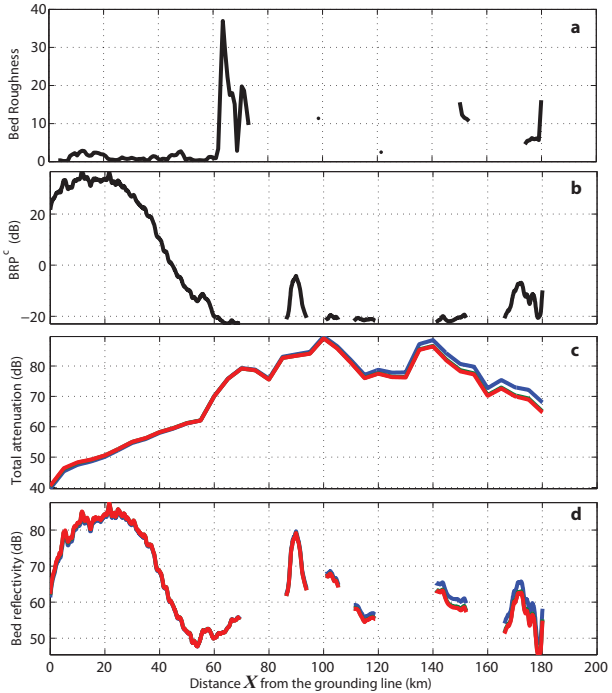

Fig. 4. Subglacial conditions along the center flowline. **(a)** Bed roughness index *RI*; **(b)** geometrically corrected bed-returned power BRP^c; **(c)** englacial attenuation *L* modelled with ice temperatures for the ice flow fields from cases A, B, and C (see text for more details); **(d)** bed reflectivity *R*. Colours for curves in panels **(c)** and **(d)** are the same as in Fig. 5.

TCD
7, 4913–4936, 2013

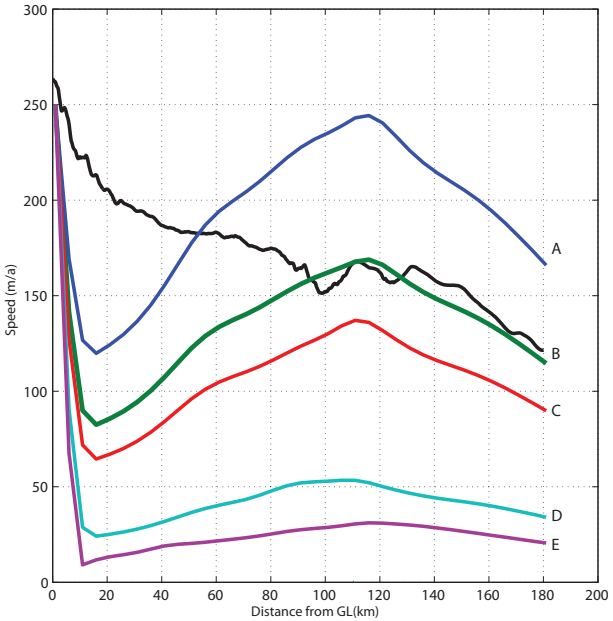

Fig. 5. Modelled (color) and observed (black) ice flow velocity along the center flowline. A–E are the five cases for different flow parameters, corresponding to englacial temperatures of −2, −4, −5, −10, and −15 °C, respectively (Cuffey and Paterson, 2010).

TCD
7, 4913–4936, 2013